

Simultaneous lesion and neuroanatomy segmentation in Multiple Sclerosis using deep neural networks

Richard McKinley^a, Rik Wepfer^a, Fabian Aschwanden^a, Lorenz Grunder^a,
Raphaela Muri^a, Christian Rummel^a, Rajeev Verma^b, Christian Weisstanner^c,
Mauricio Reyes^e, Anke Salmen^d, Andrew Chan^d, Franca Wagner^a, Roland
Wiest^a

^a*Support Center for Advanced Neuroimaging, University Institute for Diagnostic and
Interventional Neuroradiology, Inselspital, Bern University Hospital, Switzerland*

^b*Department of Neuroradiology, Spital Tiefenau, Switzerland*

^c*Medizinisch Radiologischen Institut, Zurich, Switzerland*

^d*Univeristy Clinic for Neurology, Inselspital, Bern University Hospital, Switzerland*

^e*Insel Data Science Centre, Inselspital, Bern University Hospital, Switzerland*

Abstract

Segmentation of both white matter lesions and deep grey matter structures is an important task in the quantification of magnetic resonance imaging in multiple sclerosis. Typically these tasks are performed separately: in this paper we present a single segmentation solution based on convolutional neural networks (CNNs) for providing fast, reliable segmentations of multimodal magnetic resonance images into lesion classes and normal-appearing grey- and white-matter structures. We show substantial, statistically significant improvements in both Dice coefficient and in lesion-wise specificity and sensitivity, compared to previous approaches, and agreement with individual human raters in the range of human inter-rater variability. The method is trained on data gathered from a single centre: nonetheless, it performs well on data from centres, scanners and field-strengths not represented in the training dataset. A retrospective study found that the classifier successfully identified lesions missed by the human raters.

Lesion labels were provided by human raters, while weak labels for other brain structures (including CSF, cortical grey matter, cortical white matter,

Email address: `richard.mckinley@insel.ch` (Richard McKinley)

cerebellum, amygdala, hippocampus, subcortical GM structures and choroid plexus) were provided by Freesurfer 5.3. The segmentations of these structures compared well, not only with Freesurfer 5.3, but also with FSL-First and Freesurfer 6.0.

Keywords: Deep Learning, Multiple Sclerosis, MRI

1. Introduction

MR-based imaging biomarkers are an integral part of the diagnosis and follow-up of multiple sclerosis for more than 20 years [1]. During this time, there has been a constant development of advanced methods to further improve diagnostic accuracy, establish prognosis and outcome, and leverage clinical monitoring of patients with MS. Established biomarkers for MS include baseline MRI lesion count, temporal evolution of lesion load, including the formation of new lesions, as well as the integrity of the blood brain barrier, signatures of axonal damage, and atrophy of cortical and subcortical grey matter. These measures of progression are routinely assessed by expert human readers. [2]. In the PRISMS long-term follow up study in patients with remitting-relapsing MS, higher brain volume at baseline was identified as a prognostic imaging markers for better outcome and decreased likelihood to convert into secondary progressive multiple sclerosis [3]. MRI volumes at baseline and T2-lesion burden have also been found to correlate with disability outcomes in previous studies. [4, 5, 6]. Recent evidence has suggested to monitor disease progression either by segmentation and quantification of T2 lesion load (reflecting inflammatory disease activity) or whole brain volume loss on T1-weighted images (reflecting ongoing neurodegeneration). Both measures are biomarkers for the prediction of disease progression and the efficacy of disease modifying treatment regimens. Based on a survey on the prospectively collected MSBase cohort on 8311 MRI scans with new lesions during follow up, it could be demonstrated that treatment decisions rely mainly on MRI monitoring and that subclinical T2 lesion progression was associated with increased odds of treatment change, with every new T2 lesion increasing

the odds ratio of treatment change within 12 months by 1.26 [7].

There is a considerable variance in lesion quantification between expert readers with different backgrounds (e.g. neuroradiologists vs. neuroimmunologists), and also substantial intra-rater variation. [8] Automated methods are by their nature repeatable, and an increasing number of publications have therefore investigated machine learning methods to solve the problem of unbiased lesion quantification. A previous survey of MS lesion segmentation methods showed that the majority of approaches were employing either Expectation-Maximization or k-nearest-neighbours methods.[9] Unsupervised techniques such as Expectation-Maximization and Maximum A Priori estimation remain well-accepted methodologies for brain lesion segmentation.[10, 11] More recently, improvements in hardware and software have enabled fast training and application of deep convolutional neural networks (CNNs), leading to a number of deep-learning approaches to brain segmentation. CNN-based approaches were the winning entries in several segmentation challenges over the last years. [12, 13, 14]. The low availability of high quality training data annotated by expert raters means that transferability is of high importance: a classifier trained on data from a single or small number of centers must be able to operate well on data from centres and scanners not seen during training. It is often the case that CNN-based methods do not have this property: performance is substantially degraded on external data, with retraining on additional labelled data from the external centre being required before good performance is reestablished.[15] Valverde and coworkers (2018) analyzed the effect of domain adaptation on their proposed CNN-based MS lesion segmentation method and investigated the transferability of the CNN model when applied to other MRI scanners and protocols, evaluating the minimum number of annotated images needed from the new domain and the minimum number of layers needed to re-train to obtain comparable accuracy. Performance without domain adaptation was substantially degraded. Domain adaptation was progressively more effective with increasing training cases, but the models still yielded a remarkably high performance on reduced training sets, such as a single training case.

Deep learning has also been applied to the segmentation of healthy brains. Initial attempts relied on the small numbers (30) of hand labelled brains, while later attempts have leveraged the availability of large cohorts of imaging data by training on the outputs of existing (non-learning-based) automated tools such as Freesurfer and FSL-FIRST [16, 17]. Segmentation of deep-white matter structures is highly relevant in multiple sclerosis, since a recent study of 1,417 MS patients has shown links between deep grey matter volume loss and worsening condition in multiple sclerosis.[18]. In that study, segmentation of the grey-matter structures was not carried out directly, since the tool used (FSL-FIRST) is known to be biased by the presence of white-matter lesions. Instead, the white-matter lesions were first identified using a freely available tool [19] and removed from the imaging using 'lesion filling', after which segmentations of the relevant structures were prepared.

In this paper, we propose a new deep learning method performing a simultaneous segmentation of both lesions and grey-matter structures, trained on a combination of lesion segmentations produced by expert raters, and weak labels for the healthy-appearing tissue provided by an existing automated method (Freesurfer). We hypothesize that the segmentation of these additional structures together with lesions does not negatively, and may in fact positively, impact the quality of the lesion segmentation.

2. Methods

2.1. Study design and overview

We analyzed 122 fully anonymized MRI datasets of patients with remitting-relapsing multiple sclerosis that were identified from the MS cohort databank of the MS cohort of the University of Bern. Ethical approval for the study was granted by the local ethical commission (Cantonal Ethical Commission Bern, 'MS segmentation disease monitoring', approval number 2016-02035). For direct comparison with other centers, we included a second dataset of ten fully anonymized MRI datasets from the Radiology Center Bethanien/ZH. All pa-

tients included in this dataset had provided a general consent for data storage and analysis of their MRI datasets (CW).

2.2. Patient cohorts and MR imaging

Two cohorts of retrospective data were included in the analysis: 90 datasets were included in the Insel90 dataset (used for training and validation of the classifier), and 32 patients were included in the Insel32 dataset (used in this paper for testing the classifier). All datasets stemmed from patients who fulfilled the diagnostic criteria (revised McDonald criteria of 2010) for relapsing-remitting multiple sclerosis. [20] Datasets from the Inselel hospital were acquired using a standardized acquisition protocol on a 3T MRI (Siemens Verio, Siemens, Erlangen, Germany) following the Revised Recommendations of the Consortium of MS Centers Task Force for a Standardized MRI Protocol and Clinical Guidelines for the Diagnosis and Follow-Up of Multiple Sclerosis.[3] The protocol settings included i) T1-weighted MDEFT pre- and post gadobutrol i.v. (Repetition time TR = 7.92 ms, echo time TE = 2.48 ms, flip angle = 16, inversion with symmetric timing (inversion time 910 ms), 256 x 224 x 176 matrix points with a field of view (FOV) of 256 mm x 224 mm yielding a nominal isotropic resolution of 1 mm³, with fat saturation), ii) T2-weighted imaging (TR 6580 ms, TE 85 ms, averages 2, FoV read 220 mm, FoV phase 87.5 %, voxel size 0.7 x 0.4 x 3.0 mm, flip angle 150, acquisition time 6:03 min, 42 parallel images were acquired with a slice thickness of 3.0 mm, iii) 3D FLAIR imaging (TR 5000 ms, TE 395 ms, averages 1, FoV read 250 mm, FoV phase 100 %, voxel size 1.0 x 1.0 x 1.0 mm, acquisition time 6:27 min. A total of 176 parallel images were acquired with a slice thickness of 1.0 mm). All patients received Gadobutrol (Gadovist) 0.1 ml kg⁻¹ bodyweight immediately after the acquisition of the unenhanced T1w sequence.

Anonymized training data from patients who had given informed consent was taken for testing from a second centre. (Radiology Center Bethanien) Datasets were acquired on a 3T MRI (Siemens Skyra, Siemens, Erlangen, Germany). i) T1-weighted MPRAGE precontrast (TR 2300 ms, TE 2.9 ms, TI 900 ms,

averages 1, FoV read 250 mm, FoV phase 93.75 % voxel size 1.0 x 1.0 x 1.0 mm, flip angle 9, acquisition time 05:12 min. 176 slices per slab, slice thickness of 1.0 mm) ii) T2- weighted imaging (TR 4790 ms, TE 100 ms, averages 1, FoV read 220 mm, FoV phase 100 %, voxel size 0.7 x 0.4 x 3.0 mm, flip angle 150, acquisition time 02:16 min, 45 parallel images were acquired with a slice thickness of 3.0 mm, iii) 3D FLAIR imaging (TR 5000 ms, TE 398 ms, TI 1800 ms, averages 1, FoV read 250 mm, FoV phase 100 %, voxel size 1.0 x 1.0 x 1.0 mm, flip angle 120, acquisition time 04:17 min. A total of 176 slices per slab were acquired with a slice thickness of 1.0 mm).

This dataset from Zurich, together with training data from the MSSEG challenge [14] was used to assess centre- and scanner-independence. The datasets belonging to the MSSEG challenge conform to the OFSEP guidelines, which ensures a 3D FLAIR acquisition and a 3D T1 acquisition: we consider this a minimum for high-quality multiple sclerosis imaging [21]. Briefly, 15 datasets were obtained from three different centres in France, each using a different scanner (Siemens Verio 3T, Siemens Aera 1.5T, and Philips Ingenia 3T). The images were annotated by seven trained junior experts: their segmentations were fused to provide a single ground-truth for training purposes (the 38 similar cases used for the testing phase of the MSSEG competition were not available at the time this manuscript was prepared).

2.3. Manual segmentation

MS lesion annotation of the Insel90 and Insel32 datasets was conducted by two of the authors (RWe/FA), under the supervision of an experienced neuro-radiologist with more than 15 years experience in MS reading (RWi). Manual segmentation labels of the MS lesions were acquired through slice-by-slice analysis of all four sequences. The 3DSlicer platform [22] was used to perform the manual lesion segmentation following the protocol in [23]. Lesions were identified if appearing hyper-intense compared to the surrounding normal-appearing WM on T2w and FLAIR images, and slightly- to severely hypo-intense on T1-weighted images. One of the authors (RWe) annotated the severely T1 hypo-

intense 'black holes' as an additional label.

As has previously been reported, inter-rater error for manual segmentation of multiple sclerosis lesions is very high. For this reason, a further segmentation of the cases was made by one of the authors (RM), supervised by an experienced neuroradiologist with more than 10 years of experience (FW) who had access to the initial segmentations. In this way, both false negative identifications (missed lesions) and false positive identifications (healthy appearing tissue marked as lesion) could be omitted. This multi-reader 'consensus' segmentation between three raters was used for training and validation of the classifier.

The Zürich10 dataset was labelled by a Neuroradiologist with 9 years of experience (CW), following same segmentation protocol. [23].

2.4. Weak label generation using Freesurfer

Segmentations of the cortical grey matter, cortical white matter, ventricles, cerebellum, thalamus, caudate, putamen, pallidum, hippocampus, amygdala, brain stem, ventral DC, choroid plexus, corpus callosum and accumbens area, were extracted from the volumetric segmentation (aseg.mgz) generated by applying Freesurfer 5.3 to the MDEFT acquisition. No label distinction was made between left and right hemispheres. In addition to these healthy-appearing tissue labels, Freesurfer also generated labels for white-matter hypointensities, which encompass not only lesions due to multiple sclerosis, but also the 'caps and 'bands': age-related physiological changes in the periventricular regions (mild ependymal loss, subependymal gliosis and widened extracellular space.

2.5. Baseline methods: Nabla-Net and SPM Lesion Segmentation Toolbox

As a baseline CNN-based MS lesion segmentation algorithm we use Nabla-net [12]. Nabla-net was the winning lesion segmentation algorithm in the 2016 MSSEG challenge at MICCAI: on the unseen testing data of the challenge the method achieved a mean Dice coefficient of 0.59. An important component of the challenge was to assess performance on out-of-sample data: fifteen training

examples were provided from three different centres, each using a different scanner/sequence parameters. Testing data was also taken from those three centres, together with data from a fourth centre/scanner which was unseen during training: also on this unseen centre, Nbla-net was the best-performing method.[14]¹

As an additional, freely available baseline, we applied the two lesion segmentation methods available in the Lesion Segmentation Toolbox (LST, available at <https://www.applied-statistics.de/lst.html>).[19] The toolbox is integrated into SPM, and provides two segmentation algorithms: a lesion prediction algorithm (LPA), operating on FLAIR imaging alone, and a lesion growth algorithm (LGA), operating on FLAIR and T1 imaging. As recommended by the authors of the toolkit, we used our training cases to determine the best initial threshold for the LGA algorithm.

2.6. The DeepSCAN architecture

For the classification of lesions and healthy appearing tissue, we use a cascade of two convolutional neural networks (CNNs).

In a first step, a convolutional neural network is used to individually skull-strip the T1, T2 and FLAIR images in their native spaces. Subsequently, the skull-stripped T1 and T2 images are registered to the FLAIR space using a rigid transformation (FSL-FIRST, 6 degrees of freedom, mutual information cost function, spline interpolation) and resampled to $1mm^3$ resolution: a second convolutional network is then applied to this multi-modal data to generate the final segmentation. We used a two-stage approach to provide more robustness against differences in the appearance of non-brain tissue (caused, for example, by the use of a head-only coil vs. a head-and-neck coil).

The two CNNs used in this paper both follow the DeepSCAN architecture introduced in [24]. A DeepSCAN network consists of initial 3D convolution layers, then a U-net style encoder/decoder network [25] with a dense block

¹For a detailed breakdown of the results for individual methods, see the supplementary material to Commowick et. al [14]: <https://zenodo.org/record/1307653>

[26] of dilated convolutions at the bottleneck. The shape of a network of this architecture can therefore be specified by:

- The number of initial 3D convolutions
- The depth of the encoder/decoder (i.e. the number of downsampling steps)
- The topology of the dense block: how many dense units, and at what dilation.

We describe in detail the used network topologies for skull-stripping and segmentation in the appendix.

2.7. CNN for Brain extraction

Brain masks were prepared for the 122 T1-weighted MRIs in our training and test dataset, using FSL-BET with hand-tuned parameters. These brain masks were then transferred to the T2 and FLAIR images using rigid registration by FSL-FLIRT. Brain images (T1, T2 and FLAIR) were standardized as follows:

- Calculation of 1st and 99th percentile of voxels with non-zero intensity, and clipping of images to those intensities.
- Standardisation: calculation of mean and standard deviation of voxels with non-zero intensity: subtraction of mean and division by standard deviation across all voxels.

We then trained a DeepSCAN network to predict the BET brain-mask of an axial, sagittal or coronal slice from T1, T2 or FLAIR imaging. The network used had no 3D convolutions, a depth of 3 and had two dense units with dilation 1 and two dense units with dilation 2.

2.8. CNN for segmentation

The input data to the segmentation algorithm consists acquisitions of of T1-weighted, T2 and FLAIR sequences. Before learning or prediction, these volumes are minimally pre-processed as follows:

- Skull-stripping of the FLAIR, T1 and T2 imaging, using the above-described network, and cropping to remove empty voxels.
- Rigid registration of the skull-stripped T1 and T2 images to the skull-stripped FLAIR image, using FSL-FLIRT, and resampling to 1mm isovoxels.
- Calculation of 1st and 99th percentile of brain-tissue intensities (within brain mask), and clipping of images to those intensities.
- Standardisation: calculation of mean and standard deviation of voxels within brain mask: subtraction of mean and division by standard deviation across all voxels.

In particular, no bias field correction was made to the input images, as it has been shown to adversely affect the appearance of images with large white-matter lesion load. [27]

We generated a segmentation label map for training by registering the Freesurfer-derived segmentation to the 1mm isovoxel resampled FLAIR volume (using the previously calculated rigid transformation, nearest neighbour interpolation), and overlaying the lesion maps provided by the third 'consensus' segmentation, and the T1-hypointense 'black-hole' maps, onto the weak tissue labels provided by Freesurfer. This results in a "ground truth" consisting of eighteen tissue maps, each of which will be predicted by the classifier, plus a nineteenth 'background' class, representing voxels not lying in any of the tissue classes in the label map.

We trained a DeepSCAN network with two 3D convolutions, a depth of 1 and 24 dense units (6 each at dilation levels 1,2,4 and 8). We utilized the following hybrid loss function:

1. For each target tissue class, a focal loss term with γ equal to 2. [28]
2. For each target tissue class, a focal label-flip loss term with γ equal to 2 [29]

3. A multi-class focal loss term, where the logit of the background class is set to 0.

The purpose of using focal loss (rather than ordinary binary or categorical cross-entropy loss function) is to improve performance on tasks with a very small ratio of voxels in the tissue class to voxels in the background class. The focal label-flip loss, in which the classifier estimates the probability of misclassification for each voxel and tissue class, has previously been shown to improve convergence of networks used for brain segmentation. [29] In addition, the uncertainty estimates themselves are used in a companion paper to identify patients with lesion growth in longitudinal imaging. [30] Definitions of the loss functions used in this paper are reproduced in the appendices.

The raw classifier output is an 18-element vector (x_1, \dots, x_{18}) , for each voxel in the volume, in which each element x_i of the vector represents the log-odds (or logit) of the given volume element being in one of the 18 tissue classes. Tissue "probabilities" (i.e. a number between zero and one) can be obtained from the log-odds by applying the logistic function. During training a joint loss function was minimized, consisting of the sum of the binary cross-entropies for each tissue class separately, together with the softmax loss of the vector $(0, x_1, \dots, x_{18})$, where the initial zero represents the logit of the background class. As a result of this hybrid loss function, the classifier can be used in two distinct ways for segmenting a given tissue class. Firstly, we may obtain segmentations of each tissue class individually, by thresholding the logit maps:

DeepSCAN multi-task: a voxel is labelled as being in tissue class i if x_i is greater than zero (corresponding to a probability greater than 0.5).

In this mode, each segmentation task is treated separately (one-vs-all segmentation). It is therefore possible that a given voxel may be assigned more than one tissue class (i.e. x_i and x_j may both be greater than zero for distinct i and j). This may occur due to partial volume effects, conflicting information from the multimodal data, or input data outside of the parameters given by the training data.

If exactly one label is desired for each voxel, we may simply take the strongest signal among the x_i :

DeepSCAN softmax: a voxel is labelled as being in tissue class i if x_i is the greatest among $(0, x_1, \dots, x_{18})$.

Note that this approach differs from the traditional softmax, in that the empty tissue label is assigned a default value of 0. This ensures that if none of the tissue classes is well predicted, the classifier returns an empty label.

Training of the classifier was performed using the ADAM optimizer, with a cosine-annealing learning rate schedule applied over each epoch [31]. The batch size was two, with each $4*5*192*192$ block being randomly sampled in either an axial, coronal or sagittal direction from one of the training examples. The classifier was trained on 50 cases taken from the Insel90 dataset, with the remaining 40 cases being used to validate performance of the classifier during training. The classifier was trained for 50 epochs without the label-uncertainty loss, and for another 50 with the label-uncertainty loss.

When applied to a new case, the classifier is applied in the axial, coronal and sagittal direction. Ensembling of these three outputs is then performed by averaging the logits.

In order to test whether the inclusion of the additional tissue classes had an effect on lesion segmentation, we also trained a version of the DeepSCAN classifier with the same architecture but only two tissue classes (lesion and black hole). We refer to this below as DeepSCAN (just lesions).

2.9. Identification of irreversible axonal damage: by segmentation vs by intensity

Lesions which equal the signal intensity of CSF on T1w images are referred to as 'black holes'. These areas resemble areas of axonal damage. Since a black-hole label was provided during training the DeepSCAN model, this model can be used to identify such lesions. We also propose a complementary method for identifying black-holes. The mean and standard deviation of the T1-weighted image intensity in the ventricles was calculated, and a value of the mean plus

two standard deviations was defined as a cutoff for CSF-isointense tissue. All tissue annotated by the classifier as lesion tissue, and also CSF-isointense, was labelled as black hole.

2.10. Testing

Testing of the new lesion segmentation methods (DeepSCAN lesion only, DeepSCAN multi-task and DeepSCAN softmax) and the baseline methods (Nabla-net, and two methods from the Lesion Segmentation Toolkit (LST)) was performed against the consensus manual segmentation on the Insel32 dataset by three methods: Dice coefficient, lesion detection and volume difference.

In addition, we evaluated our proposed methods on the MSSEG training data and the ZH10 data, to establish performance on data from different centres, scanners and field strengths.

2.10.1. Dice coefficient

The *Dice coefficient*, also known as the Dice-Sørensen coefficient or Dice Similarity score, is a standard measure of segmentation agreement. If X and Y are two sets, the Dice coefficient is defined as

$$\text{Dice}(X, Y) = \frac{2|X \cap Y|}{|X| + |Y|} \quad (1)$$

We calculated, for each testing case and each segmentation method, the Dice coefficient between the lesion segmentation and the consensus segmentation. We also calculated the Dice coefficient between the individual raters, and between each individual rater and the consensus lesion segmentation, to give an impression of the inter-rater error. Dice coefficient was also used to rate the quality of secondary segmentation targets. We compared three methods of identifying T1 black holes: the black hole label supplied by DeepSCAN multi-task, the black hole label supplied by DeepSCAN softmax, and the black hole label supplied by identifying CSF-isointense areas in the DeepSCAN multi-task FLAIR lesions, using Dice coefficient relative to the single manual rater. While the main purpose of the weak labels for neuroanatomical structures is to reduce levels of false positive lesion identification in healthy-appearing tissue, we

also report Dice coefficient between our algorithm and three existing automated approaches: Freesurfer 5.3 (the source of the weak labels), Freesurfer 6.0 and FSL-FIRST.

2.10.2. Lesion detection rates

In addition to assessing the quality of voxel-by-voxel detection of lesion tissue, we also assess detection at the lesion level. We follow the proposed lesion detection metrics of the MSSEG 2016 challenge, for reference see Commowick et al. [14].

A "lesion" in a given segmentation will be defined as a connected component of the segmentation (with 18-connectivity kernel) of size $3mm^3$ or greater. We use the notation $D_X(Y)$ to stand for the detection rate of X -lesions in the segmentation Y , meaning the proportion of lesions in X successfully detected by Y . For these purposes, a lesion in X is detected by Y if:

- The lesion overlaps with lesions in Y by at least $\alpha\%$.
- The lesions which contribute most to the detection of the lesion (those summing up to $\gamma\%$ of the overlap) do not lie more than $\beta\%$ outside the lesion.

A lesion can thus fail to be detected either by "undersegmenting" (the lesion is missed, or is detected but the corresponding lesions in Y are too small), or by "oversegmenting" (the corresponding lesions in Y are too large). We adopt the values $\alpha = 10$, $\beta = 70$, $\gamma = 65$ from [14]. The value $D_X(Y)$ is then simply the ratio of the number of lesions detected to the total number of lesions in X . If X is the "ground truth" and Y is any other segmentation, then $D_X(Y)$ measures the proportion of true lesions which were correctly segmented, or sensitivity, of the segmentation Y . In this case, $D_Y(X)$ is the proportion of lesions segmented by Y which are in "true lesions", i.e. the *precision* or Positive Predictive Value.

2.10.3. Analysis of False Positives and False negatives

Since manual annotation of MS lesions is at risk of large inter-rater variability, we hypothesize that for a robust classifier differences between classifier

output and manual annotations are more likely errors in the manual annotation, than errors of the classifier.[8] To assess the extent to which this is true, two raters (FW and LG) made a final assessment of each false positive lesion (i.e. labelled by the algorithm but not overlapping the ground truth by more than 10%), and each false negative lesion (i.e. labelled in the ground truth but not overlapping with the segmentation of the algorithm by more than 10%). The raters were blind to whether the lesion segmentation came from the manual raters or the algorithm. The goal was to identify what proportion of 'false positive' lesions were in fact missed by all three raters, and what proportion of 'false negative' lesions were in fact mislabelled (i.e. were normal-appearing grey matter, choroid plexus, or the result imaging artifacts).

2.10.4. Lesion Volumetry

Finally, we assessed lesion volumetry, both by correlation and Bland-Altman analysis. For comparison, we provide the performance also for our previous lesion-segmentation method, Nabla-Net.

3. Results

3.1. Lesion segmentation on the Insel32 dataset

3.1.1. Dice coefficient

The mean Dice coefficient between the two individual raters was 0.58 (standard deviation 0.17), while the mean Dice coefficient between the raters and the human-derived consensus was 0.63 (s.d. 0.12) and 0.57 (s.d. 0.20) respectively.

The mean Dice coefficient of lesion segmentation derived from DeepSCAN against the human-derived consensus was 0.57 (s.d. 0.16) when segmenting lesions only, 0.60 (s.d. 0.12) when using multi-task classification, and 0.59 (s.d. 0.14) when using softmax classification. For comparison, the mean Dice coefficient of lesion segmentation derived from our previous algorithm (Nabla-net) against the human-derived consensus was 0.49 (s.d. 0.19). Box plots of the distribution of Dice scores can be seen in Figure 4, together with performance of LGA and LPA.

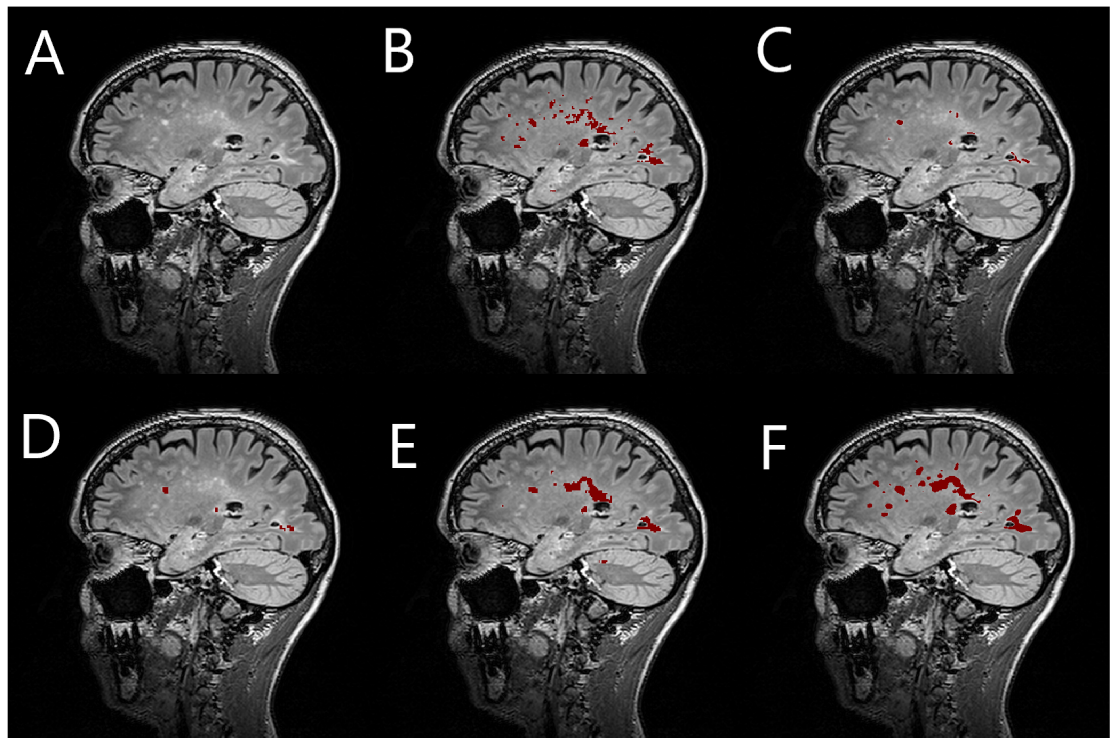


Figure 1: Example segmentations of a case from the Insel32 dataset, sagittal view. (A) FLAIR image, plus segmentations from (B) manual raters, (C) LPA, (D) LGA, (E) Nabla-net and (F) DeepSCAN (multi-task)

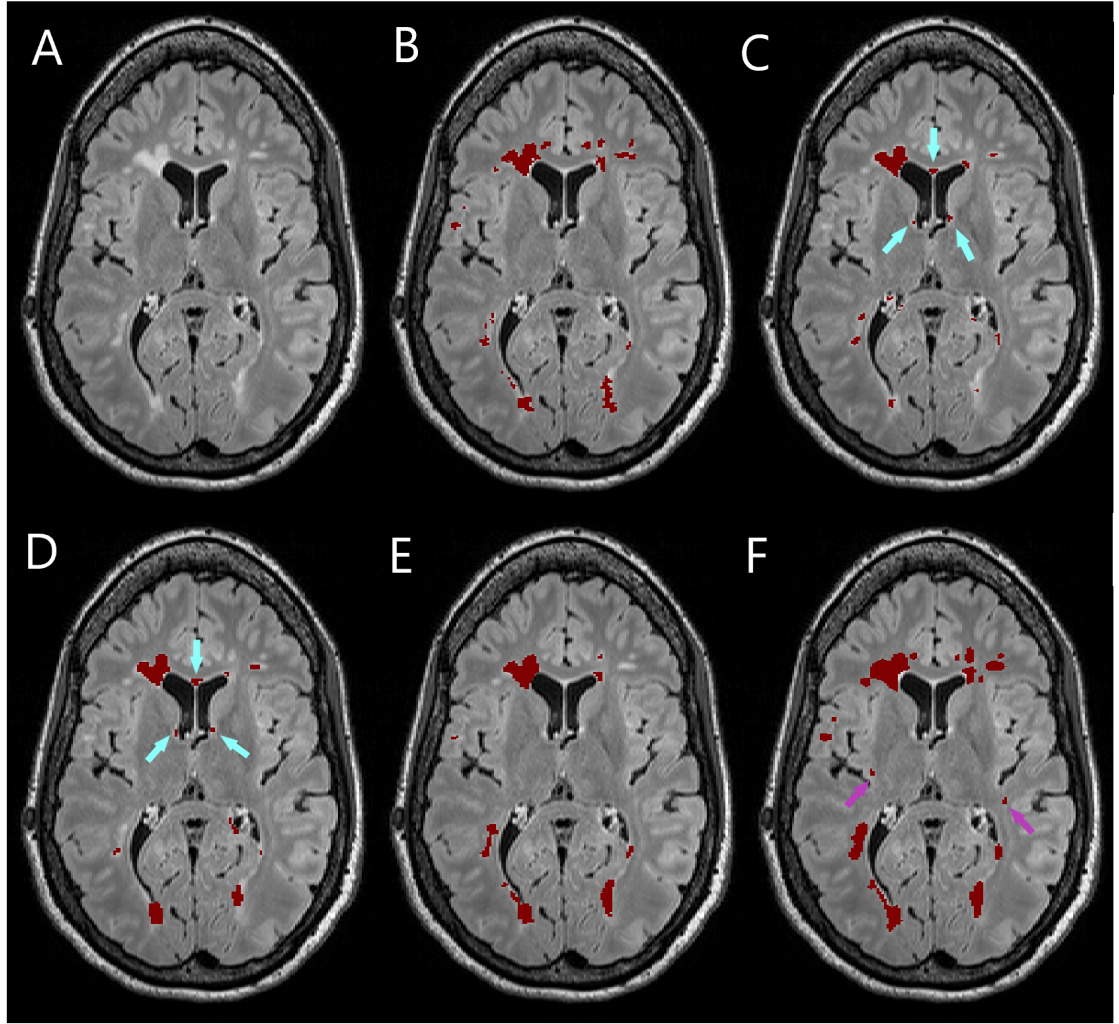


Figure 2: Example segmentations of a case from the Insel32 dataset, axial view. (A) FLAIR image, plus segmentations from (B) manual raters, (C) LPA, (D) LGA, (E) Nabla-net and (F) DeepSCAN (multi-task). Segmentations from LGA and LPA show erroneous segmentation of healthy-appearing tissue near the ventricles (cyan arrows). DeepSCAN identified two subtle lesions (violet arrows) missed by the manual raters but subsequently confirmed by our experienced neuroradiologists.

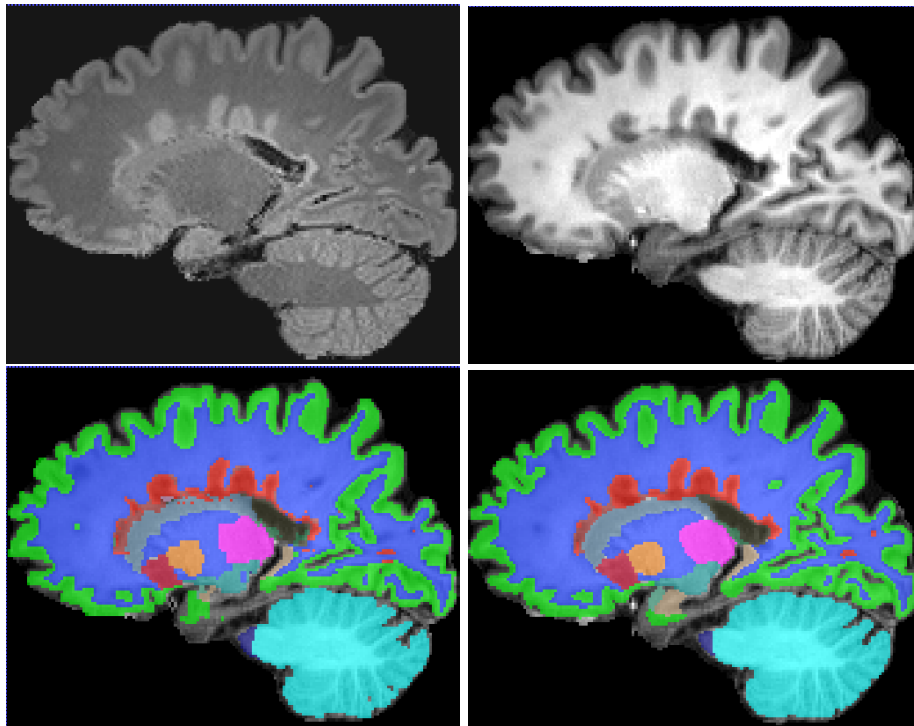


Figure 3: A sagittal slice from a case in the Insel32 dataset. Top left, FLAIR, Top right, T1 MDEFT, bottom left, fused 'ground truth', bottom right, DeepSCAN softmax output. Labels derived from the DeepSCAN tool are smoother and more anatomically plausible than those derived from Freesurfer.

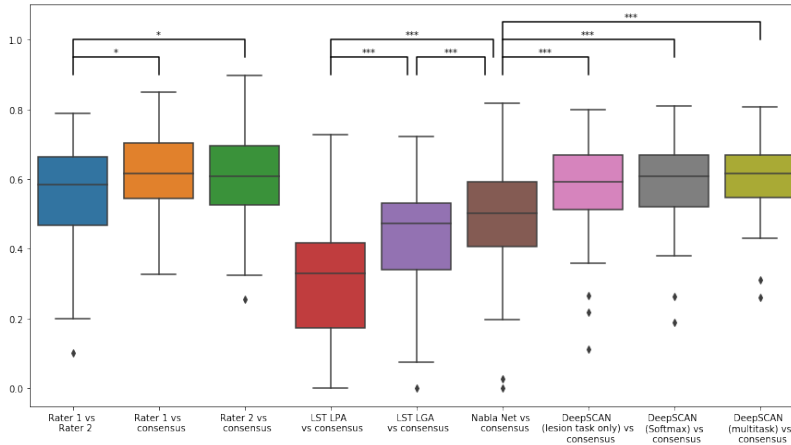


Figure 4: Boxplots showing Dice coefficients of the lesion segmentation on the Insel32 dataset. Significance levels refer to Wilcoxon signed Rank tests. Not shown: Nabla-net vs Consensus is significantly different to Rater 1 vs Rater 2, Rater 1 vs Consensus, and Rater 2 vs Consensus. LPA vs consensus is significantly worse than all shown methods. LGA vs consensus is significantly worse than all shown methods except LPA.

Wilcoxon signed rank tests show that the Dice coefficients between the human consensus and Nabla-net are significantly different to those between DeepSCAN (multi-task) and the human consensus ($p < 1e - 5$) and to those between DeepSCAN (softmax) and the human consensus ($p < 1e - 5$). In terms of Dice coefficient comparisons with the human consensus, no significant difference was found between the three segmentations of DeepSCAN (lesion only, multi-task and softmax), or between the segmentations of DeepSCAN and the individual human raters.

3.1.2. Lesion detection

Over all 32 test subjects in the Insel32 dataset, there were a total of 2701 lesions annotated in the consensus labelling. Of those lesions, 509 were successfully detected by Nabla-net, 1333 by DeepSCAN (softmax) and 1355 by DeepSCAN (multi-task). Nabla-net annotated 1153 structures as being lesions, of which 385 were present in the consensus labeling. DeepSCAN (softmax) annotated 1927 structures as lesions, of which 1204 were present in the consensus

labelling. 2019 lesions structures were annotated by DeepSCAN (multi-task) as lesions, of which 1366 were present in the consensus labeling.

In summary, over the Insel32 dataset, Nabla-net had a sensitivity of 0.19, and a precision of 0.34, DeepSCAN (softmax) had a sensitivity of 0.49 and a precision of 0.62, and DeepSCAN (multi-task) had a sensitivity of 0.50 and a precision of 0.68. The distributions of per-patient sensitivity, precision and F1 score are displayed by the boxplots in Figure 5, together with performance of LGA and LPA.

All three segmentations offered by the DeepSCAN had F1 scores, sensitivity and precision superior that offered by Nabla-net (Wilcoxon signed rank test, $p < 1e - 6$). Between the DeepSCAN segmentations, the multi-task segmentation had significantly better precision ($p = 0.003$) and F1 score ($p=0.0008$) than the softmax segmentation, but the two did not have significantly different sensitivities ($p= 0.014$). DeepSCAN (multitask) also had significantly better F1 ($p=0.003$) and sensitivity ($p=0.0006$) than DeepSCAN (just lesions).

3.1.3. Restrospective classification of false positives/negatives

Of the 2701 lesions in the consensus ground truth, the multi-task classifier failed to find 777 (a further 569 were oversegmented). However, in the retrospective lesion analysis, 579 out of those 777 (75%) were judged by a pair of trained neuroradiologists working together as being mislabelled (i.e. were normal-appearing grey matter, choroid plexus, or the result imaging artifacts).

Of the 2019 lesions annotated by DeepSCAN multi-task, 372 did not overlap more than 10% with lesions in the consensus ground truth. In the retrospective lesion analysis, 137 of those lesions (37%) were judged to be genuine lesions which had been missed by the manual raters. Among those missed lesions were several subtle cortical lesions, such as the one depicted in Figure 6.

3.1.4. Detection/segmentation of T1 hypointense ‘black holes’

Boxplots of the Dice coefficient over the Insel32 dataset for black hole segmentation are shown in Figure 7. Wilcoxon signed rank tests showed no signif-

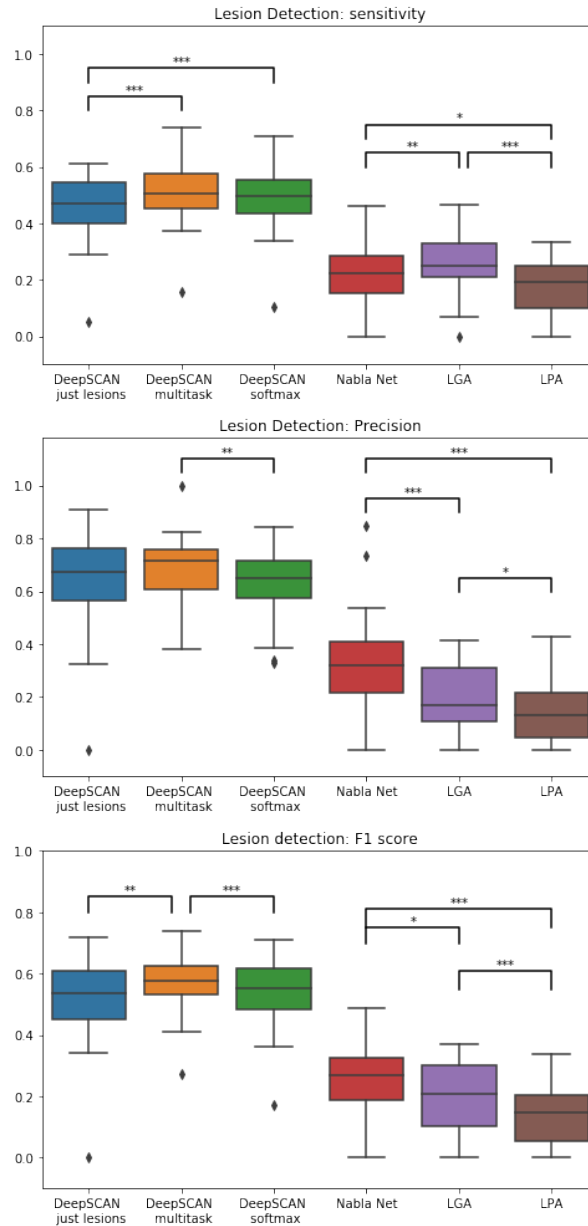


Figure 5: Boxplots showing lesion detection metrics on the Insel32 dataset. Significance levels refer to Wilcoxon Signed Rank test. Not shown: in all plots, LGA, LPA and Nabla-net are significantly worse than the three DeepSCAN methods ($p < 10^{-6}$).

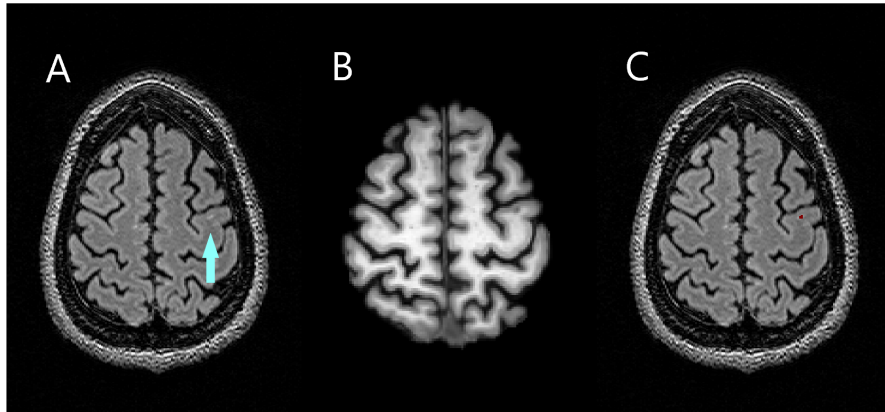


Figure 6: Example of a subtle cortical lesion from the Insel32 dataset found by DeepSCAN but missed by all raters. (A) FLAIR image: no lesions were annotated by any raters on this slice, but cortical region indicated is hyperintense (B) coregistered skull-stripped T1 image of the same slice, showing T1 hypointensity in the location of suspect lesion. (C) Segmentation from DeepSCAN, correctly identifying the missing cortical lesion.

icant difference between DeepSCAN binary and the T1w-intensity method for identifying Black holes, while both of those methods were significantly better than DeepSCAN softmax.

3.2. Segmentation of healthy-appearing grey matter structures on the Insel32 dataset

An example of the whole-brain segmentation generated by DeepSCAN Softmax can be seen in Figure 3, and boxplots of the Dice coefficient for the segmentation (DeepSCAN multi-task) of various grey-matter structures, when compared with three freely available tools (FSL-FIRST, Freesurfer 5.3, and Freesurfer 6.0) can be found in Figure 8. In two cases (Putamen and Pallidum), the Dice coefficients between DeepSCAN and Freesurfer 5.3 (which supplied the training data) were significantly better than those with Freesurfer 6.0 and FSL-FIRST. In the other five cases, at least one of FSL-FIRST or Freesurfer 6.0 compared better with the output of DeepSCAN than Freesurfer 5.3. In general, as can be seen in Figure 3, the boundaries of the structures segmented

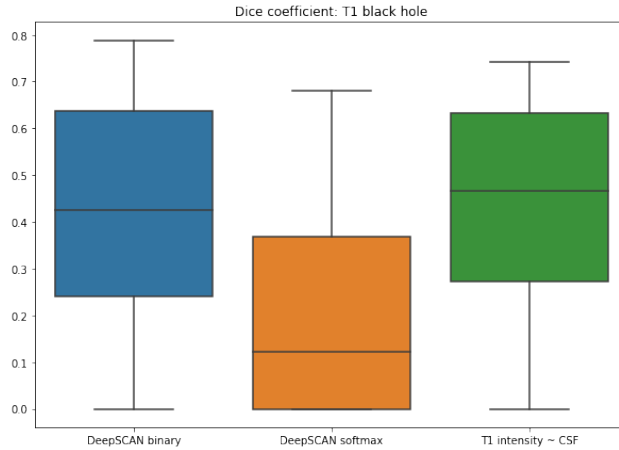


Figure 7: Distribution of the Dice Coefficients for T1 black hole segmentation, .

by DeepSCAN are smoother and more anatomically plausible than those generated by Freesurfer. Mean Dice coefficient for each structure, and each reference method, exceeded the Dice coefficient for lesion segmentation, suggesting that strong spatial priors make these structures easier to segment.

3.3. Testing of Centre/Scanner robustness

We applied our newly developed lesion segmentation algorithm to smaller datasets from different centres, and on different scanners, to evaluate the robustness of our method to new out-of-sample data.

3.3.1. MSSEG Challenge Training data

For each of the fifteen training cases of the MSSEG challenge, the organizers provided seven manual segmentations, plus a consensus segmentation. Our reference method, Nabla-net, was trained on these fifteen cases, so we refer in this section to the cross-validated performance of Nabla-net (train on ten cases, test on the remaining five).

Mean Dice coefficients versus the fused ground-truth for DeepSCAN multi-task, DeepSCAN softmax and Nabla-net were 0.66, 0.66 and 0.67 respectively. Mean F1 lesion detection scores were 0.55, 0.55 and 0.49 respectively. Wilcoxon

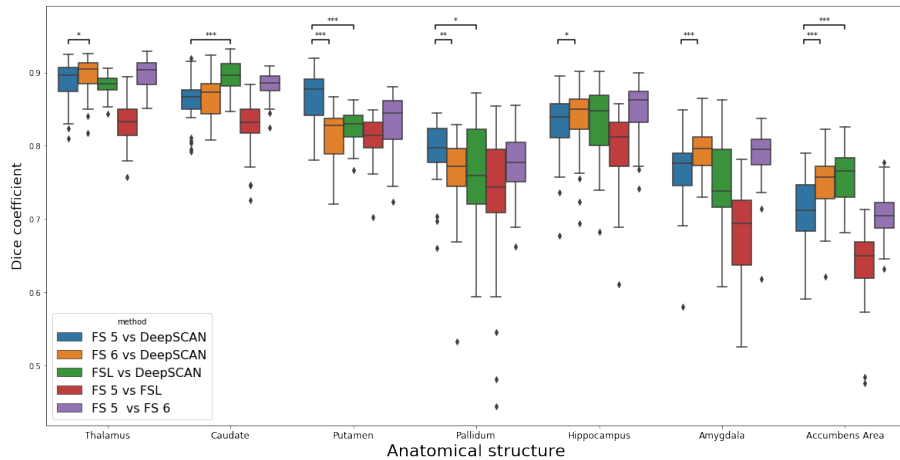


Figure 8: Boxplots of Dice coefficients for various automatic segmentations of grey-matter structures. Significance levels refer to Wilcoxon signed rank tests between FS5 vs DeepSCAN and the other automated methods.

signed rank tests showed no significant difference between the three methods on either score, meaning that the DeepSCAN methods, trained on out-of-sample, performed as well as Nabla-net trained on data from the same distribution as the test data.

Versus the independent MSSEG raters, mean agreement ranged between 0.56 and 0.61 for both DeepSCAN multitask and DeepSCAN softmax, and between 0.55 and 0.62 for Nabla-net. For comparison, the mean Dice coefficient between the MSSEG raters on the training data ranged between 0.54 and 0.75: in other words, both Nabla-net and DeepSCAN performed within the inter-rater range of performance, when measuring Dice coefficients.

3.3.2. Zurich10 dataset

Mean Dice coefficient for DeepSCAN multi-task on this dataset was 0.51, and mean Dice coefficient for DeepSCAN Softmax was 0.52. Mean lesion detection F1 for DeepSCAN multi-task on this dataset was 0.48, and mean lesion detection F1 for DeepSCAN softmax was 0.48. Wilcoxon signed rank tests found no difference between the two methods on this dataset.

3.4. Lesion volumetry

Bland-Altman plots of DeepSCAN (multi-task) and DeepSCAN (softmax) for the task of lesion segmentation, compared with the consensus segmentation, across all three test datasets (Insel32, Zurich10 and MSSEGG) are shown in Figure 9. The softmax segmentation showed no trend with increasing volume, and little bias, while the multi-task network showed a bias towards larger lesion load than the human raters, and a statistically significant ($p = 2e - 5$) trend.

4. Discussion

We proposed a new classifier for MS lesion segmentation, in which lesion segmentation performance is improved by simultaneous labelling of healthy-appearing structures, reducing the number of false positive and false negative identifications. We demonstrated substantial improvements in lesion-wise false positive and false negative rates over existing methods, and robustness across vendors and centres.

We compared the performance of our proposed method with an award-winning lesion segmentation algorithm from a recent segmentation challenge.[14] When compared with the cross-validated performance of the reference method trained the multi-centre training set from that challenge (MSSEG), no significant difference in results was found between DeepSCAN and Nabla-net, the best performing method in terms of Dice coefficient on the 2016 MSSEG testing set, suggesting that adequate performance on multi-centre/scanner data can be derived from training on single-centre data. When applied to held-out test data from our institution, the proposed method performed significantly better than the reference method, in terms of Dice coefficient, sensitivity, and precision of lesion segmentation. In particular, lesion-wise sensitivity, precision and F1 score scores for the proposed method were twice those of the baseline. Performance was similar on data coming from a second centre in Switzerland, and performance on the training data from the MSSEG challenge was similar to the performance of an award-winning baseline method trained on in-sample data:

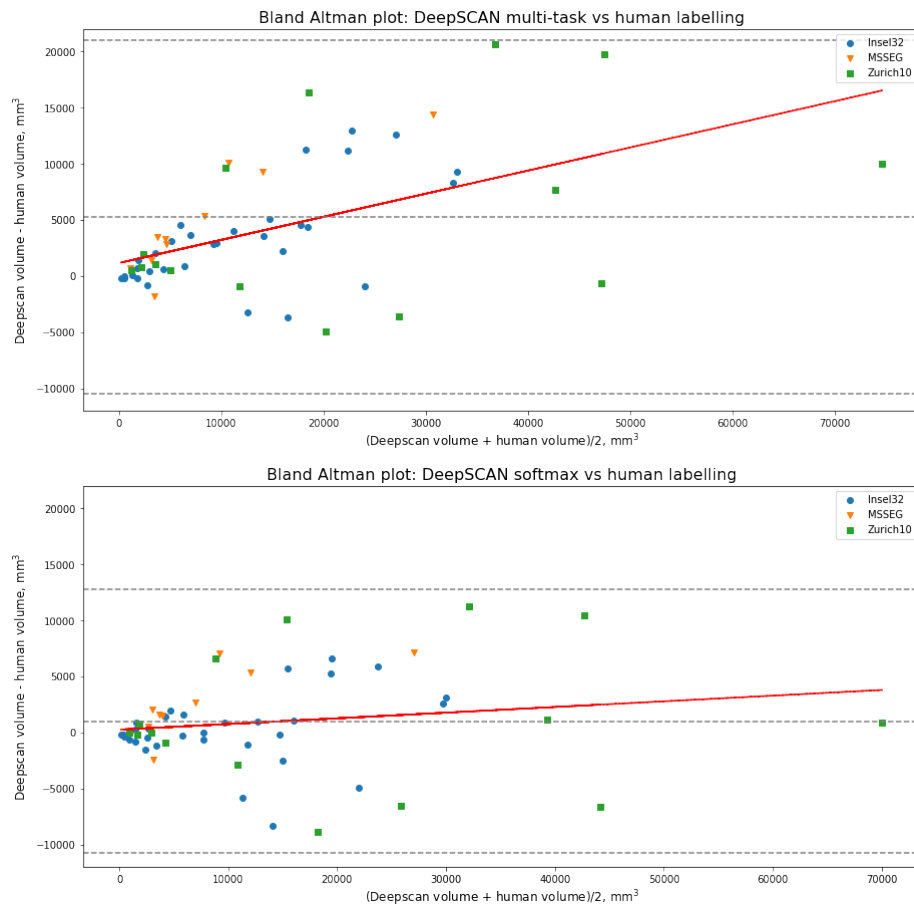


Figure 9: Bland-Altman plots comparing automated and human lesion volumetry on the InseI32, MSSEG and Zurich datasets. Trendline shown in red for each case. The softmax segmentation showed no significant trend in volumetric difference ($p=0.22$), while the multi-task segmentation showed a significant positive trend (slope = 0.2, $p=2e-5$)

we did not see the reduction in performance on out-of-sample data reported for other methods.

The method also provides segmentations, and so volumetry, of cortical grey matter and deep grey matter structures. Segmentation quality, when measured by Dice coefficient, did not show a bias towards the training data: while the automated labelling was generated from Freesurfer 5.3, agreement with Freesurfer 5.3 was lower than with Freesurfer 6 in 5 out of seven structures examined, and was lower than agreement with FSL FIRST in three out of seven structures examined. This suggests that the classifier is not merely reproducing the segmentation of Freesurfer 5.3. One obvious exception to this trend is Putamen segmentation, where the method agreed substantially more with Freesurfer 5.3 than with the other two methods. This can, perhaps, be explained by a known issue with Freesurfer 5.3, where the segmentation of the putamen intrudes into the claustrum: this also led to low agreement between Freesurfer 5.3 and human raters. [32].

Current assessments of segmentation algorithm quality rely on comparison either with single human raters or consensus segmentations derived from multiple raters. Typically, consensus segmentations are preferred because of the high inter-rater variability of MS lesion segmentation: on the MSSEG training dataset, for example, mean Dice coefficients between the independent expert raters ranges between 0.75 and 0.54. Meanwhile the agreement between DeepSCAN and the individual MSSEG raters was between 0.57 and 0.61, showing that our performance is within the range of human inter-rater variability. Performance on the MSSEG training dataset, which was not used for training our classifier, was not significantly worse than the cross-validated performance of Nbla-net. Performance on an additional external validation set was also similar to the performance on our internal validation set, suggesting that domain adaptation may be less crucial when applying our method to data from different clinics. This contrasts to previously reported results, where performance on data from previously unseen centres was substantially degraded without domain adaptation [15].

Our post-hoc examination of missed and oversegmented lesions showed that, despite substantial efforts to produce a robust ground truth segmentation, 579 lesions (out of a total of 2701) in the test set were found to be mislabelled healthy-appearing tissue. Meanwhile, of the 2019 lesions annotated by DeepSCAN multitask, 137 were judged to be missed lesions (i.e. genuine lesions not present in the ground truth), and only 235 were judged to be mislabelled healthy-appearing tissue. While we can not guarantee that this method has found all false positive identifications of lesions in the segmentations, this corresponds to a roughly 11% rate of false positives for DeepSCAN, vs a 21% false positive rate for the consensus of manual raters. The fact false positive rates among a consensus of human raters is more than double that of an automated classifier shows that comparisons with human raters may, in the end, be insufficient to judge whether systems such as the one we propose can be used in clinical practice. Even in carefully curated lesion annotation datasets, the difficulty of the lesion segmentation task was such that substantial numbers of lesions were missed, and an even greater number of false positive lesion identifications were made in the 'ground truth'. In the end, these systems must be validated independently of comparing to human raters, as a biomarker for disease progression. Nonetheless, our results show that it is possible to train classifiers even on such noisy ground truths. In a companion paper, we show that by using measures of uncertainty derived from the loss function of our classifier, we can distinguish between stable and progressive timepoints in relapsing-remitting MS.

While clinical practice is shifting towards low threshold treatment change if a single new, clinically silent T2 lesion is detected, most routine investigations still omit grey matter atrophy as an early and reproducible feature of MS. Several studies consistently demonstrated a link between atrophy, disease progression and cognitive dysfunction, yielding differences between different MS phenotypes. Grey matter atrophy is present from the earliest stages of multiple sclerosis, spreading consistently across multiple sclerosis phenotypes and involving increasing numbers over time.[33] Covariance analysis of regional grey matter atrophy may inform the determination of altered network topology among dif-

ferent MS phenotypes. Such new network metrics depend on accurate and fast region-wise volumetric measures and constitute an new class of biomarkers for the neurodegenerative component of multiple sclerosis. While in this paper, we do not address regional grey matter atrophy, segmentations of the cortical grey matter are produced as one of the compartments segmented by our proposed method. Together with registration to an atlas this method can therefore produce regional volumetric measures. Furthermore, by applying a method such as DiReCT, measures of cortical thickness can be extracted from the tissue maps produced by DeepSCAN.[34, 35].

As well as potential clinical impact, the tool we have developed has the potential to improve other neuroimaging studies. For example, in order to measure the volumes of subcortical structures of MS patients in a recent study, it was necessary to first automatically segment the lesions, then perform lesion filling, and finally segment the relevant structures. [18] By contrast, using our proposed method the segmentations of subcortical structures could be derived directly: alternatively, if established tools for the segmentation of subcortical structures are preferred, our lesion segmentation provides a more complete identification of the lesion load than previously available tools.

There are several limitations of the study which may be improved in subsequent work. The major limitation is that the labels of healthy-appearing structures are derived from, and compared to, other automated tools (Freesurfer5.3/6.0 and FSL-FIRST). A more useful comparison would be between our automated tool and manual expert labels. One could also expect that a tool trained on better quality labels would perform better in such a comparison, and it would be instructive to compare performance on of a classifier trained on small, human-labelled datasets versus those trained on larger weakly labelled datasets, as well as methods combining the two.

Another limitation of the current study is our attention only to cross-sectional data. In a companion study [30], we propose to look at longitudinal imaging of the same Insel32 dataset, in order to demonstrate the viability of automated methods for reliably detecting changes in lesion loads. Improved labelling (weak

or human-derived) of the healthy-appearing tissue, in particular the cortex, would allow such methods to be applied also to atrophy biomarkers.

Finally, while we validated our methodology on a number of datasets, including one publicly available challenge training dataset, we believe that the best basis for the comparison of methods such as the one we propose is the provision of challenges, in which methods are applied to hidden testing datasets independently of the challenge participants. As an alternative, for groups unwilling or unable to participate in challenges, it is essential that those groups who can release their methods to provide a baseline for further development: we intend to prepare the method presented in this paper for distribution for this purpose.

4.0.1. Acknowledgements

This research was supported by the Swiss Multiple Sclerosis Society and a grant from the Novartis Forschungsstiftung.

References

References

- [1] H. F. McFarland, J. A. Frank, P. S. Albert, M. E. Smith, R. Martin, J. O. Harris, N. Patronas, H. Maloni, D. E. McFarlin, Using gadolinium-enhanced magnetic resonance imaging lesions to monitor disease activity in multiple sclerosis, *Annals of Neurology* 32 (????) 758–766.
- [2] J. J. Graber, S. Dhib-Jalbut, Biomarkers of disease activity in multiple sclerosis., *Journal of the neurological sciences* 305 1-2 (2011) 1–10.
- [3] A. Traboulsee, J. Simon, L. Stone, E. Fisher, D. Jones, A. Malhotra, S. Newsome, J. Oh, D. Reich, N. Richert, K. Rammohan, O. Khan, E.-W. Radue, C. Ford, J. Halper, D. Li, Revised recommendations of the consortium of ms centers task force for a standardized mri protocol and clinical guidelines for the diagnosis and follow-up of multiple sclerosis, *American Journal of Neuroradiology* 37 (2016) 394–401.

- [4] D. S. Goodin, A. Traboulsee, V. Knappertz, A. T. Reder, D. Li, D. Langdon, C. Wolf, K. Beckmann, A. Konieczny, G. C. Ebers, Relationship between early clinical characteristics and long term disability outcomes: 16 year cohort study (follow-up) of the pivotal interferon β -1b trial in multiple sclerosis., *J. Neurol. Neurosurg. Psychiatry* 83 (2012) 282–7.
- [5] A. Langer-Gould, R. A. Popat, S. M. Huang, K. Cobb, P. Fontoura, M. K. Gould, L. M. Nelson, Clinical and demographic predictors of long-term disability in patients with relapsing-remitting multiple sclerosis: a systematic review., *Arch. Neurol.* 63 (2006) 1686–91.
- [6] P. A. Brex, O. Ciccarelli, J. I. O’Riordan, M. Sailer, A. J. Thompson, D. H. Miller, A longitudinal study of abnormalities on MRI and disability from multiple sclerosis., *N. Engl. J. Med.* 346 (2002) 158–64.
- [7] M. Min, T. Spelman, A. Lugaresi, C. Boz, D. L. Spitaleri, E. Pucci, F. GrandMaison, F. Granella, G. Izquierdo, H. Butzkueven, J. L. Sanchez-Menoyo, M. Barnett, M. Girard, M. Trojano, P. Grammond, P. Duquette, P. Sola, R. Alroughani, R. Hupperts, S. Vucic, T. Kalincik, V. V. pesch, J. Lechner-Scott, Silent lesions on mri imaging shifting goal posts for treatment decisions in multiple sclerosis, *Multiple Sclerosis Journal* 24 (2018) 1569–1577. PMID: 30234431.
- [8] E. Erbayat Altay, E. Fisher, S. Jones, C. Hara-Cleaver, J.-C. Lee, R. Rudick, Reliability of classifying multiple sclerosis disease activity using magnetic resonance imaging in a multiple sclerosis clinic 70 (2013) 338–44.
- [9] D. Mortazavi, A. Kouzani, H. Soltanian-Zadeh, Segmentation of multiple sclerosis lesions in mr images: A review 54 (2011) 299–320.
- [10] S. Jain, A. Ribbens, D. M. Sima, M. Cambron, J. De Keyser, C. Wang, M. H. Barnett, S. Van Huffel, F. Maes, D. Smeets, Two time point ms lesion segmentation in brain mri: An expectation-maximization framework, *Frontiers in Neuroscience* 10 (2016) 576.

- [11] M. Fartaria, A. Todea, T. Kober, K. O'brien, G. Krueger, R. Meuli, C. Granziera, A. Roche, M. Bach Cuadra, Partial volume-aware assessment of multiple sclerosis lesions, *NeuroImage : Clinical* 18 (2018) 245–253.
- [12] R. McKinley, R. Wepfer, T. Gundersen, F. Wagner, A. Chan, R. Wiest, M. Reyes, Nabla-net: A deep dag-like convolutional architecture for biomedical image segmentation, in: A. Crimi, B. Menze, O. Maier, M. Reyes, S. Winzeck, H. Handels (Eds.), *Brainlesion: Glioma, Multiple Sclerosis, Stroke and Traumatic Brain Injuries*, Springer International Publishing, Cham, 2016, pp. 119–128.
- [13] S. Valverde, M. Cabezas, E. Roura, S. Gonzalez-Villa, D. Pareto, J. C. Vilanova, L. Ramio-Torrenta, A. Rovira, A. Oliver, X. Llado, Improving automated multiple sclerosis lesion segmentation with a cascaded 3D convolutional neural network approach, *Neuroimage* 155 (2017) 159–168.
- [14] O. Commowick, A. Istace, M. Kain, B. Laurent, F. Leray, M. Simon, S. Camarasu-Pop, P. Girard, R. Améli, J.-C. Ferré, A. Kerbrat, T. Tourdias, F. Cervenansky, T. Glatard, J. Beaumont, S. Doyle, F. Forbes, J. Knight, A. Khademi, A. Mahbod, C. Wang, R. McKinley, F. Wagner, J. Muschelli, E. Sweeney, E. Roura, X. Llado, M. M. Santos, W. P. Santos, A. G. Silva-Filho, X. Tomas-Fernandez, H. Urien, I. Bloch, S. Valverde, M. Cabezas, F. J. Vera-Olmos, N. Malpica, C. Guttman, S. Vukusic, G. Edan, M. Dojat, M. Styner, S. K. Warfield, F. Cotton, C. Barillot, Objective evaluation of multiple sclerosis lesion segmentation using a data management and processing infrastructure, *Accepted, Nature Scientific Reports*, 2018 (2018).
- [15] S. Valverde, M. Salem, M. Cabezas, D. Pareto, J. C. Vilanova, L. Ramió-Torrentà, A. Rovira, J. Salvi, A. Oliver, X. Lladó, One-shot domain adaptation in multiple sclerosis lesion segmentation using convolutional neural networks, *NeuroImage. Clinical* (2018) 101638.
- [16] C. Wachinger, M. Reuter, T. Klein, Deepnat: Deep convolutional neural

network for segmenting neuroanatomy, *NeuroImage* 170 (2018) 434 – 445.
Segmenting the Brain.

- [17] M. Rajchl, N. Pawlowski, D. Rueckert, P. M. Matthews, B. Glocker, Neuronet: Fast and robust reproduction of multiple brain image segmentation pipelines, *CoRR abs/1806.04224* (2018).
- [18] A. Eshaghi, F. Prados, W. J. Brownlee, D. R. Altmann, C. Tur, M. J. Cardoso, F. De Angelis, S. H. van de Pavert, N. Cawley, N. De Stefano, M. L. Stromillo, M. Battaglini, S. Ruggieri, C. Gasperini, M. Filippi, M. A. Rocca, A. Rovira, J. Sastre-Garriga, H. Vrenken, C. E. Leurs, J. Killestein, L. Pirpamer, C. Enzinger, S. Ourselin, C. A. G. Wheeler-Kingshott, D. Chard, A. J. Thompson, D. C. Alexander, F. Barkhof, O. a. Ciccarelli, Deep gray matter volume loss drives disability worsening in multiple sclerosis, *Annals of Neurology* 83 (????) 210–222.
- [19] P. Schmidt, C. Gaser, M. Arsic, D. Buck, A. Frschler, A. Berthele, M. Hoshi, R. Ilg, V. J. Schmid, C. Zimmer, B. Hemmer, M. Mhlau, An automated tool for detection of flair-hyperintense white-matter lesions in multiple sclerosis, *NeuroImage* 59 (2012) 3774 – 3783.
- [20] C. H. Polman, S. C. Reingold, B. Banwell, M. Clanet, J. A. Cohen, M. Filippi, K. Fujihara, E. Havrdova, M. Hutchinson, L. Kappos, F. D. Lublin, X. Montalban, P. O’Connor, M. Sandberg-Wollheim, A. J. Thompson, E. Waubant, B. Weinshenker, J. S. Wolinsky, Diagnostic criteria for multiple sclerosis: 2010 revisions to the mcdonald criteria, *Annals of Neurology* 69 (????) 292–302.
- [21] F. Cotton, S. Kremer, S. Hannoun, S. Vukusic, V. Dousset, Ofsep, a nationwide cohort of people with multiple sclerosis: Consensus minimal mri protocol, *Journal of Neuroradiology* 42 (2015) 133 – 140.
- [22] A. Fedorov, R. Beichel, J. Kalpathy-Cramer, J. Finet, J.-C. Fillion-Robin, S. Pujol, C. Bauer, D. Jennings, F. Fennessy, M. Sonka, J. Buatti, S. Ayward, J. V. Miller, S. Pieper, R. Kikinis, 3d slicer as an image computing

- platform for the quantitative imaging network, *Magnetic Resonance Imaging* 30 (2012) 1323 – 1341. Quantitative Imaging in Cancer.
- [23] D. García-Lorenzo, S. J. Francis, S. Narayanan, D. L. Arnold, D. L. Collins, Review of automatic segmentation methods of multiple sclerosis white matter lesions on conventional magnetic resonance imaging, *Medical image analysis* 17 1 (2013) 1–18.
- [24] R. McKinley, A. Jungo, R. Wiest, M. Reyes, Pooling-free fully convolutional networks with dense skip connections for semantic segmentation, with application to brain tumor segmentation, in: A. Crimi, S. Bakas, H. Kuijff, B. Menze, M. Reyes (Eds.), *Brainlesion: Glioma, Multiple Sclerosis, Stroke and Traumatic Brain Injuries*, Springer International Publishing, Cham, 2018, pp. 169–177.
- [25] O. Ronneberger, P. Fischer, T. Brox, U-Net: Convolutional Networks for Biomedical Image Segmentation, *Medical Image Computing and Computer-Assisted Intervention – MICCAI 2015* (2015) 234–241.
- [26] G. Huang, Z. Liu, L. van der Maaten, K. Q. Weinberger, Densely connected convolutional networks, in: *Proceedings of the IEEE Conference on Computer Vision and Pattern Recognition*.
- [27] M. d. C. Valdés Hernández, V. González-Castro, D. T. Ghandour, X. Wang, F. Doubal, S. Muñoz Maniega, P. A. Armitage, J. M. Wardlaw, On the computational assessment of white matter hyperintensity progression: difficulties in method selection and bias field correction performance on images with significant white matter pathology, *Neuroradiology* 58 (2016) 475–485.
- [28] T.-Y. Lin, P. Goyal, R. B. Girshick, K. He, P. Dollár, Focal loss for dense object detection, *2017 IEEE International Conference on Computer Vision (ICCV)* (2017) 2999–3007.
- [29] R. McKinley, M. Rebsamen, R. Meier, M. Reyes, C. Rummel, R. Wiest, Few-shot brain segmentation from weakly labeled data with

deep heteroscedastic multi-task networks, arXiv e-print, available at <https://arxiv.org/abs/1904.02436> (2019).

- [30] R. McKinley, L. Grunder, R. Wepfer, F. Aschwanden, T. Fischer, C. Friedli, R. Muri, C. Rummel, R. Verma, C. Weisstanner, M. Reyes, A. Salmen, A. Chan, R. Wiest, F. Wagner, Automatic detection of lesion load change in multiple sclerosis using convolutional neural networks with segmentation confidence, arXiv e-print, available at <https://arxiv.org/abs/1904.03041> (2019).
- [31] I. Loshchilov, F. Hutter, SGDR: stochastic gradient descent with restarts, CoRR abs/1608.03983 (2016).
- [32] G. Perlaki, R. Horvath, S. Nagy, P. Bogner, T. Doczi, J. Janszky, G. Orsi, Comparison of accuracy between fsfs first and freesurfer for caudate nucleus and putamen segmentation, *Scientific Reports* 7 (2017).
- [33] A. Eshaghi, R. V. Marinescu, A. L. Young, N. C. Firth, F. Prados, M. Jorge Cardoso, C. Tur, F. De Angelis, N. Cawley, W. J. Brownlee, N. De Stefano, M. Laura Stromillo, M. Battaglini, S. Ruggieri, C. Gasperini, M. Filippi, M. A. Rocca, A. Rovira, J. Sastre-Garriga, J. J. G. Geurts, H. Vrenken, V. Wottschel, C. E. Leurs, B. Uitdehaag, L. Pirpamer, C. Enzinger, S. Ourselin, C. A. Gandini Wheeler-Kingshott, D. Chard, A. J. Thompson, F. Barkhof, D. C. Alexander, O. Ciccarelli, Progression of regional grey matter atrophy in multiple sclerosis, *Brain* 141 (2018) 1665–1677.
- [34] N. J. Tustison, P. A. Cook, A. Klein, G. Song, S. R. Das, J. T. Duda, B. M. Kandel, N. van Strien, J. R. Stone, J. C. Gee, B. B. Avants, Large-scale evaluation of ants and freesurfer cortical thickness measurements, *NeuroImage* 99 (2014) 166 – 179.
- [35] S. R. Das, B. B. Avants, M. Grossman, J. C. Gee, Registration based cortical thickness measurement, *NeuroImage* 45 (2009) 867 – 879.

- [36] S. Jégou, M. Drozdal, D. Vázquez, A. Romero, Y. Bengio, The one hundred layers tiramisu: Fully convolutional densenets for semantic segmentation, volume abs/1611.09326.
- [37] A. Kendall, Y. Gal, What uncertainties do we need in bayesian deep learning for computer vision?, in: NIPS.

Appendix A. Details of the DeepSCAN architecture and CNN training

Densenet [26] is a recently introduced architecture for image classification. The fundamental unit of a Densenet architecture is the densely connected block, or dense block. Such a block consists of a number of consecutive dense units, as pictured in Figures A.11 and A.12 . In such a unit, the output of each convolutional layer (where a layer here means some combination of convolutional filters, non-linearities and batch normalization) is concatenated to its input before passing to the next layer. The goal behind Densenet is to build an architecture which supports the training of very deep networks: the skip connections implicit in the concatenation of filter maps between layers allows the flow of gradients directly to those layers, providing an implicit deep supervision of those layers.

In the original Densenet architecture, which has state-of-the-art performance on the CIFAR image recognition task, dense blocks are combined with transition blocks: non-densely connected convolutional layers, followed by a maxpooling layer. This helps to control parameter explosion (by limiting the size of the input to each dense block), but also means that the deep supervision is not direct, at the lowest layers of the network. This Dense-plus-transition architecture was also adopted by Jegou et al. [36], whose Tiramisu network is a U-net-style variation of the Densenet architecture designed for semantic segmentation.

In a previous paper on brain tumor segmentation [24], we proposed an alternative hybrid of U-net [25] and Densenet, in which the bottleneck layer of the Unet is a single dense block, and in which some or all of the pooling and upscaling is replaced by dilated convolutions. Some kind of pooling is found in

almost all CNNs for image classification. The principal reason to use pooling is to efficiently increase the receptive field of the network at deeper levels without exploding the parameter space, but another common justification of pooling, and maxpooling in particular, is that it enables some translation invariance. Translation invariance is of course undesirable in semantic segmentation problems, where what is needed is instead translation *equivariance*: a translated input corresponding to a translated output. To that end, we use layers with dilated convolutions to aggregate features at multiple scales. Dilated convolutions, sometimes called atrous convolutions, can be best visualized as convolutional layers “with holes”: a 3 by 3 convolutional layer with dilation 2 is a 5 by 5 convolution, in which only the centre and corner values of the filter are nonzero, as illustrated in Figure A.10. Dilated convolutions are a simple way to increase the receptive field of a classifier without losing spatial information.

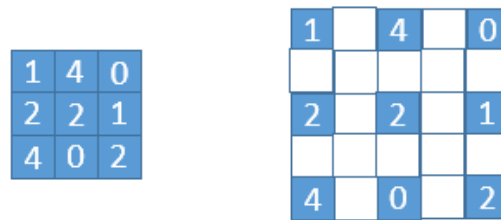


Figure A.10: Left, a 3 by 3 kernel. Right, a 3 by 3 kernel with dilation 2, visualized as a 5 by 5 kernel

The DeepSCAN network used to segment lesions and healthy-appearing brain structures in this paper is shown in Figure A.11, while the network used to for initial brain extraction is shown in Figure A.12.

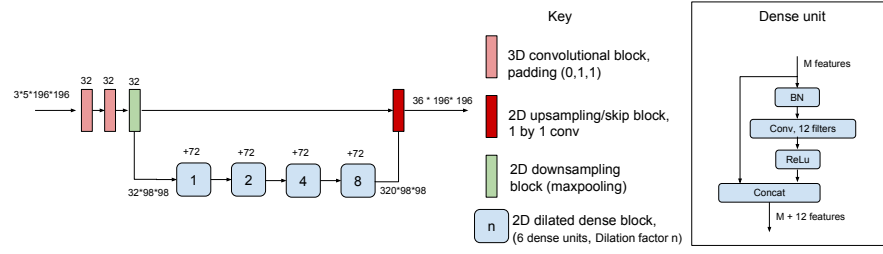


Figure A.11: The DeepSCAN architecture used in this paper for lesion and brain-structure segmentation

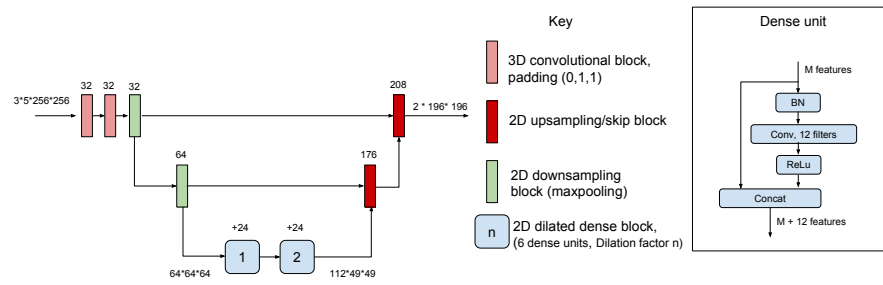


Figure A.12: The DeepSCAN architecture used in this paper for brain extraction

Appendix B. Custom loss function

The loss function we use is an unweighted combination of three individual loss functions: a focal loss function for each tissue class, a new uncertainty aware loss term for each tissue class, which estimates the probability that the predicted tissue class differs from the ground-truth label, and a slightly modified softmax loss term over all tissue classes.

i) The focal loss function of [28] was developed for situations where there is substantial class imbalance in classification problems: for MS lesions and also many neuroanatomical tissue types this is the case. The loss function works by reducing the contribution of already well-classified examples to the loss function, and is given by

$$Focal_{\gamma}(p, x) = (1 - p_x)^{\gamma}(BCE(p, x)) \quad (B.1)$$

where BCE is the standard binary cross-entropy loss, p is the output probability of the network, x is the label in the ground truth, and $p_x = x * p + (1 - x) * (1 - p)$. For the purposes of this paper we set the value of γ to be 2.

ii) label-uncertainty loss is a new loss function for binary classification allowing networks to quantify their own uncertainty. In brief, for each voxel, and each segmentation subtask (whole tumor, tumor core, and enhancing tumor) the network outputs two probabilities: the probability p that the label is positive, and the probability q that the label predicted does not correspond to the label in the ground-truth annotation (i.e., the probability of a 'label flip'). If BCE stands for the standard binary cross-entropy loss, and y is the target label, then the label-uncertainty loss is:

$$BCE(p, (1 - x) * q + x * (1 - q)) + BCE(q, z) \quad (B.2)$$

where

$$z = (p > 0.5) * (1 - x) + (p < 0.5) * x \quad (B.3)$$

If q is close to zero, and the label is correct, the first term is approximately the ordinary BCE loss: if q is close to 0.5 (representing total uncertainty as to the

correct label) the first term tends to zero. This loss therefore attenuates loss in areas of high uncertainty (i.e., where the network is often incorrect), in a similar fashion to the heteroscedastic loss of [37]. However, in [37] the uncertainty in the classification is modeled by assuming that logits have a Gaussian distribution, and estimating the variance of that Gaussian: this cannot be performed directly by gradient descent, instead requiring Monte Carlo sampling of the Gaussian distribution to perturb the output of the network. By contrast, label-uncertainty can be incorporated directly into the loss-function of the network.

In practice, since not only the labels, but also the areas of label uncertainty are in the minority we minimize the following loss function:

$$Focal_2(p, (1 - x) * q + x * (1 - q)) + Focal_2(q, z) \quad (B.4)$$

iii) Multi-class classification (in which each element, here voxel, is assigned exactly one label), is typically managed in deep learning using a Softmax non-linearity and a categorical cross-entropy loss function. For the purposes of classification the chosen class is the one with the largest output. Given outputs $\mathbf{y} = y_0, \dots, y_n$, the softmax nonlinearity returns

$$\sigma(\mathbf{y})_j = \frac{\exp(y_j)}{\sum_{i=0}^n \exp(y_i)} \quad (B.5)$$

Thus the outputs of the softmax are scaled such that they sum to one, and can be regarded as probabilities.

In cases where we insist that a label is assigned to each example, this functions well. However, it can be in a softmax that no label is predicted with high confidence: in this case the most likely label is still predicted. To avoid that this leads to erroneous/random classification of tissue as lesions we add a background class with a fixed output of 0 (corresponding to a probability of 0.5). This ensures that only voxels predicted as being lesion (or any other class) by multi-task classification will be assigned that class by softmax.